Reconstructing the Anak Krakatau flank collapse that caused the December 2018 Indonesian tsunami

Rebecca Williams[1*], Pete Rowley[1], and Matthew C. Garthwaite[2]

[1]*Department of Geography, Geology & Environment, University of Hull, Cottingham Road, Hull, HU7 6RX UK.*

[2]*Positioning and Community Safety Division, Geoscience Australia, Cnr Jerrabomberra Ave and Hindmarsh Drive, Symonston, Canberra, ACT 2609, Australia.*

**Correspondence to: Rebecca.williams@hull.ac.uk.*

ABSTRACT

Volcanogenic tsunamis are one of the deadliest volcanic phenomena. Understanding their triggering processes and mitigating their effect remains a major challenge. On 22 December 2018, flank failure of the Anak Krakatau volcano in Indonesia generated a tsunami which killed more than 400 people. This event was captured in unprecedented detail by high-resolution satellite imagery and eyewitness accounts. Here we combine historic observations with these recent data to - for the first time - interpret the internal architecture of Anak Krakatau, and reconstruct the failure, tsunamigenesis and regrowth processes observed. We calculate the volume of material initially lost from the volcano flank failure and find that it was relatively small (~0.1 km^3) compared to the overall changes observed during the entire eruption but was nonetheless able to generate rapid tsunami waves with devastating impacts. The flank failure also changed the eruption style and upper volcanic plumbing system, with these subsequent explosive eruptions destroying the summit and then partially rebuilding the lost flank. The nature of the

flank failure was controlled by the internal structure of the island, and - although regrowth rate will be a primary control on flank failure intervals - the reconfiguring of the volcano's internal vent network is likely to have re-stabilised it in the medium term. The findings demonstrate that hazard assessments at ocean islands must consider that even small flank failures, during unexceptional eruptions, can have catastrophic consequences.

INTRODUCTION

Volcanogenic tsunamis have caused the deaths of over 55,000 people since 1600 AD (Auker et al., 2013). The last three centuries have seen around 100 notable volcanogenic tsunamis produced in the world's oceans (Day, 2015). Volcanogenic tsunamis are triggered by a variety of processes, including submarine volcanic explosions, entry of volcanic flows into the ocean, sudden flank deformations, or flank failures, and are not necessarily triggered by a volcanic eruption. Their unpredictability and the high amplitude of generated waves makes volcanogenic tsunamis a significant local and regional hazard, often with catastrophic consequences (Day, 2015). However, they occur rarely and there have been very few volcanogenic tsunamis observed in sufficient detail to enable evaluation of their triggering, propagation mechanisms and their impacts (some examples are Stromboli in 2002 (Bonaccorso et al., 2003; La Rocca et al., 2004), and Soufrière Hills in 2003 (Pelinovsky et al., 2004)).

The December 2018 Indonesian Tsunami

On 22 December 2018, Anak Krakatau ('Child of Krakatau'), an active volcanic island situated within the Krakatau caldera in the Sunda Strait between Java and Sumatra, Indonesia, experienced a flank failure. This flank failure generated a volcanogenic tsunami, causing widespread damage to the surrounding coastlines (Fig. S1).

Prior to December 2018, the active volcanic cone of Anak Krakatau (6.102°S, 105.423°E) had grown to ~300 m above sea level, having first risen above sea-level in 1929 (Neumann van Padang, 1933). The caldera-forming eruption of Krakatau in 1883 caused the deaths of 36,000 people (Auker et al., 2013) after pyroclastic density currents entered the ocean and generated a catastrophic tsunami that swept the coasts of the Sunda Strait (Self and Rampino, 1981). Anak Krakatau has frequently erupted since 1927, with eruptions typically strombolian to vulcanian in style, characterized by small explosive eruptions with columns reaching to 2 km in height (Camus et al., 1987; Deplus et al., 1995; Agustan et al., 2012). Anak Krakatau is located on the edge of the steep NE wall of the 1883 Krakatau caldera (Fig S2), and its rapid growth, comprising largely of loose pyroclastic material (Fig. 1A), meant that Anak Krakatau was already recognized as an unstable edifice and tsunami risk (Giachetti et al., 2012). Prior to the flank failure, the volcano had been in an active phase since June 2018, producing strombolian eruptions.

At 21:27 Western Indonesian Time (WIB) on 22 December 2018 a tsunami impacted the coasts of the Pandeglang, Serang and South Lampung regions in Indonesia (Fig. S1). The waves ranged in height from 0.27 to 1.40 m (Fig. S1), caused the deaths of 431 people, injured a further 7,200 people, and displaced 46,646 people (Ramadhan, 2018). There has been significant damage to coastal infrastructure, including 1,778 houses, 78 damaged lodging and warung (small family owned business) units, 434 damaged boats and ships and some damage to public facilities (Press release dated 29 December 2018 15:17 UTC (BNPB)).

On the day of the tsunami, the Anak Krakatau volcano was in an elevated but unexceptional phase of activity (Andersen, Ø.L 2019), undergoing a strombolian-style eruption. An ash column of up to 1.5 km was observed, and earthquake tremors of typical amplitude were recorded (Press

release dated 23 December 2018 (MAGMA; PVMBG). A low frequency 5.1 Mw earthquake, with a NW-SE trending focal plane was recorded at 20:55 WIB on the regional seismic network ("GEOFON Program"). Further earthquake activity was recorded at 21.03 WIB and appears to have destroyed the seismometer situated on Anak Krakatau (Press release dated 23 December 2018 00:01 UTC (BNPB)). Twenty-four minutes later, the first tsunami waves reached the surrounding coasts.

Here, we: (i) reconstruct the internal architecture of Anak Krakatau prior to the tsunami-generating flank failure; (ii) calculate the volume of collapsed material; and (iii) build a conceptual model for the failure and subsequent regrowth process to mid-January 2019.

DATA AND METHODS

The flank failure was captured in unprecedented detail by remote sensing satellites. The first observation of Anak Krakatau following the flank failure was made by the Sentinel-1A Synthetic Aperture Radar (SAR) satellite, which imaged the volcano at 05:33 WIB on 23 December 2018 (22:33, 22 December 2018 UTC), only ~8 hours after the tsunami impacted the coast (Fig. 1). We combine geomorphological analysis of the SAR data (Fig. 2) with a constructed cross-section of Anak Krakatau (Fig. 3) to calculate the volume of the flank failure. Full details on the data sources and SAR processing, can be found in supplementary materials.

Cross-Sections

Bathymetric and topographic surveys from 1918, 1928, 1960 and 1990 are compiled in Figure 3, together with qualitative descriptions of the growth of the edifice, and a recent profile derived from the DEM of the volcano.

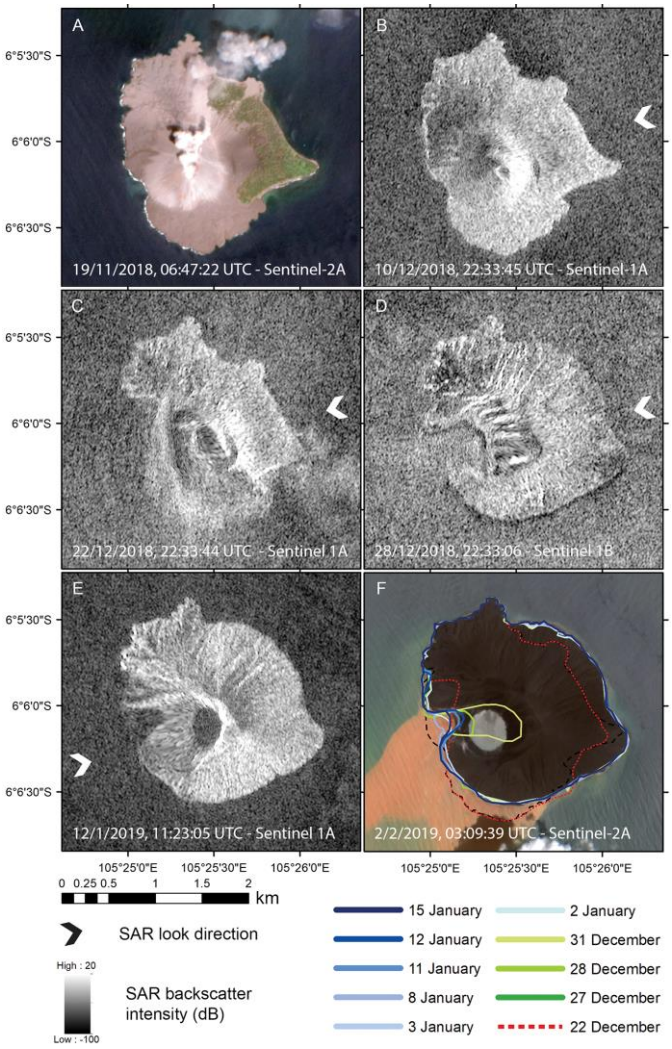

Figure 1. Satellite imagery showing the evolving geomorphology of Anak Krakatau as a result of the December – January eruptive activity and the 22 December 2018 tsunami. Panel A and B show the island morphology before the flank failure. Panel C was captured only 8 hours after the tsunami and shows the western flank failure and collapse of the summit. Panel D shows the destruction of the summit and Panel E shows the subsequent regrowth of the island. Panel F tracks the changes in island surface area through this period. Panel A and F are Sentinel-2A true colour images and panels B-E are Sentinel-1A and -1B SAR backscatter images. Arrows show the radar looking direction.

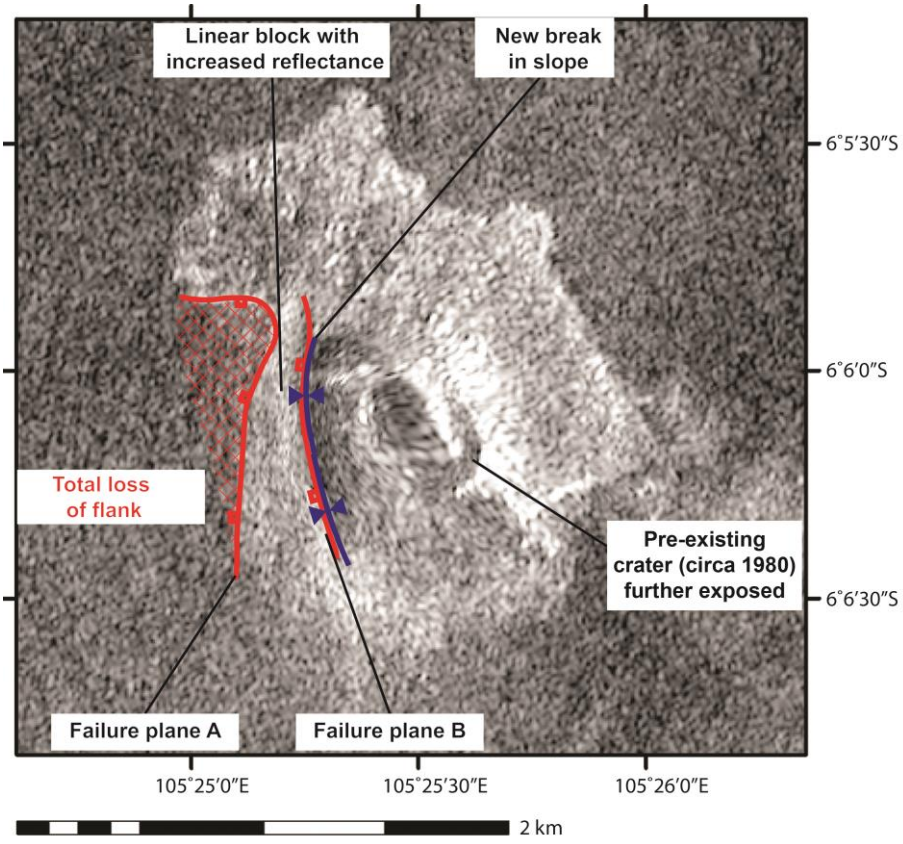

Figure 2. Interpretation of 22 December 2018 Sentinel-1A SAR image, showing two discrete failure planes; plane A which has enabled complete loss of its hanging wall material, and plane B which has resulted in a rotational slide of the linear block between the failure planes, with an undefined magnitude of slip.

Volume calculations

The subaerial failure surface area (and outlines of the evolving island shape) was delineated using a combination of Sentinel 2 visible spectrum imagery and Sentinel-1 SAR data. To calculate the subaerial volume of material mobilised in the flank failure the failed section of the DEM was isolated, and subsurface volume was calculated down to sea level using ArcGIS 3D

Analyst. Depending where the failure plane is drawn with respect to the SAR data a range of subaerial volumes is derived.

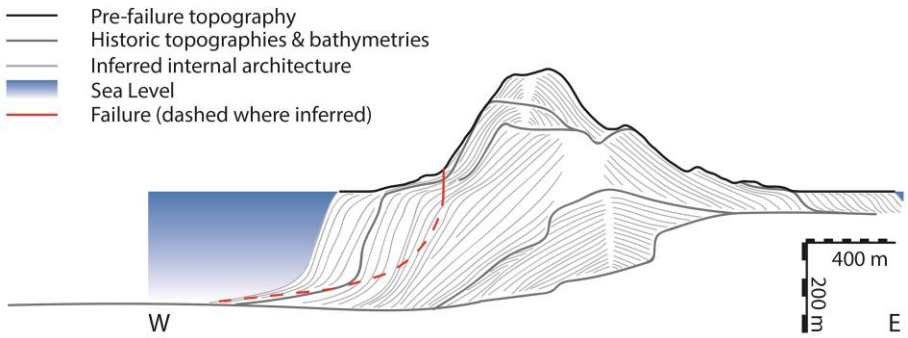

Figure 3. A west-east cross section through Anak Krakatau (2x vertical exaggeration) showing the pre-failure topography (black outline) and the reconstructed internal architecture of the volcano (grey lines). Constructed using data from (Decker and Hadikusumo, 1961; Deplus et al., 1995; Giachetti et al., 2012) and the Badan Informasi Geospasial digital elevation model. Failure plane A (solid red line) and the inferred submarine failure plane (dashed red line) for the tsunami-generating flank failure is shown, as used for the volume calculations. The proposed failure plane B and rotated block is not shown as it was not removed during the flank failure event.

For the submarine failure volume we assume the subvertical failure plane at the surface (supported by observations made by aerial photography – e.g. Fig S3), projects down into a listric failure, propagating to near the base of the modern edifice (Fig. 3) and somewhat constrained by the inferred internal architecture of the volcano. Although we have interpreted slip on a second inland plane (Fig. 2) we have not included this in volume calculations as it is impossible to constrain the orientation of the plane, or the timing or magnitude of slip with the present data. The submarine flank failure volume is calculated using analysis of the cross section

(Fig. 3) to gain a cross sectional area of collapsed volume, and simplified to a prism, with the cross sectional area multiplied by the failure length observed from SAR imagery (Fig 1c, 900 m). This will lead to a slight overestimation of volume, as we are not assuming a conical submarine stratigraphy around the summit. Ten separate interpretations and cross-sectional areas are used to derive a final value, constrained by the SAR imagery and simple listric fault geometry. However, given the assumptions in reconstructing the submarine edifice, lack of recent bathymetric data (last survey done in 1990), and poor constraints on how much material had been added or removed from the submarine edifice since 1990, we do not feel justified in stating the maximum failed volume to a precision higher than 0.1 km^3

RESULTS AND DISCUSSION

Analysis of this SAR image clearly shows that the western portion of Anak Krakatau had failed and collapsed (Fig. 1C). Subsequent images reveal significant morphological changes to the volcano as the eruption progressed (Fig. 1D-F). Here we interpret the time series of Sentinel-1 SAR images captured from three viewing geometries to understand the mechanisms of the flank failure and tsunami generation and how the volcano responded during the subsequent eruptions.

Volume of flank failure

Our interpretation of the 22 December 2018 (UTC) SAR image reveals a 900 m NNE-SSW trending linear plane along which the western flank has failed (Fig. 2, failure plane A). In addition, a new break in slope has appeared east of this failure, and the block between the failure and the summit cone exhibits increased reflectance relative to the previously captured radar image (10 December 2018 UTC). Radar backscatter intensity depends on three factors: surface geometry with respect to the incident radar; surface roughness at the scale of the radar wavelength (5.6 cm for Sentinel-1); and the dielectric properties of the surface material (Di

Traglia et al., 2018). Thus, the increased reflectance could be caused by the deposition of fresh pyroclastic material or disturbed ground. However, the feature is linear, with a sharp transition, so unlikely to be new pyroclastic material. Furthermore, erupted material would be expected to be more radially distributed around the vent. Therefore, our interpretation is that the block has rotated with partial slip along this second inland failure plane (Fig. 2, failure plane B). The head of the failing slope has rotated back toward the radar source such that it backscatters more energy, thus also explaining both the new break in slope and the higher radar reflectance. Given that the summit cone is clearly visible in the 22 December 2018 (UTC) SAR image ~8 hours after the tsunami, but that the block appears to have gone by the 28th December (Fig 1D), we conclude that it was not removed during the flank failure but during subsequent eruptive activity. The lack of a second tsunami suggests that this block did not fail as a second landslide. Initial slip and rotation of this block appears to follow the underlying structure of a pre-existing crater on which the modern summit was built (Decker and Hadikusumo, 1961; Deplus et al., 1995). The north and eastern flanks of the volcano are largely unaffected by the failure.

Cross-sections through the pre-failure edifice illuminate the nature of the failure and help constrain the total volume of lost material during this event (Fig. 3). These show that the island has grown over a basement structure formed during the collapse of the Krakatau caldera in 1883 (Deplus et al., 1995). The core of the Anak Krakatau edifice has migrated westward through time (Deplus et al., 1995; Giachetti et al., 2012), which has resulted in the bulk of the modern edifice being built on an array of strata which dip toward the center of the 1883 caldera. This gives a preferential failure direction to the west which may explain the marine inundations of the core of the island from the west (e.g. Fig. 1D-F, and (Decker and Hadikusumo, 1961)).

We calculate volumes of 0.004 km^3 (range 0.003 to 0.0045 km^3) for the subaerial failure, and in the order of 0.1 km^3 (range 0.086 - 0.093 km^3) for the submarine failure. This places the subaerial volume within the error of the submarine volume. This is small for a volcanic flank failure; terrestrial flank failures at volcanoes have had volumes up to 10 km^3, and submarine volcanic flank failures up to 5000 km^3 are known to have occurred (Watts and Masson, 1995; Voight and Elsworth, 1997; Carracedo, 1999; Carracedo et al., 1999).

Flank failure and the generation of a tsunami was a known hazard for Anak Krakatau. Giachetti et al. (2012) modelled a failure of 0.28 km^3 of the western flank, estimating wave heights on the coastlines of the Sunda Strait ranging from 0.3 m to 3.4 m. Our estimate of the 2018 flank failure is much smaller in volume (3x smaller; ~0.1 km^3). However, for three locations, the waves were as high as those modelled by Giachetti et al. The waves arrived on the coasts of Java and Sumatra within 24-37 minutes, 10 minutes quicker than modelled for Java and over 20 minutes quicker than modelled for Sumatra (Giachetti et al., 2012). Hence, the speed of the tsunami waves were substantially underestimated in the model and future tsunami hazard assessments for the Sunda Strait must consider these more rapid wave velocities.

Reconstruction of eruptive activity following tsunami generation

The flank failure was followed by a significant change in subsequent eruptive activity (Fig. 4) and migration of the eruption vent multiple times between 22 December 2018 and 12 January 2019. Following the failure, aerial photography taken on 23 December 2018 (Fig. S3) shows an eruptive column centered offshore of the failure scarp. We propose that the flank failure decompressed the plumbing system sufficiently that a new magma pathway was opened, which resulted in a new submarine vent ~500 m west of the pre-existing vent. This allowed the incursion of water into the vent, producing the violent phreatomagmatic eruptions observed on

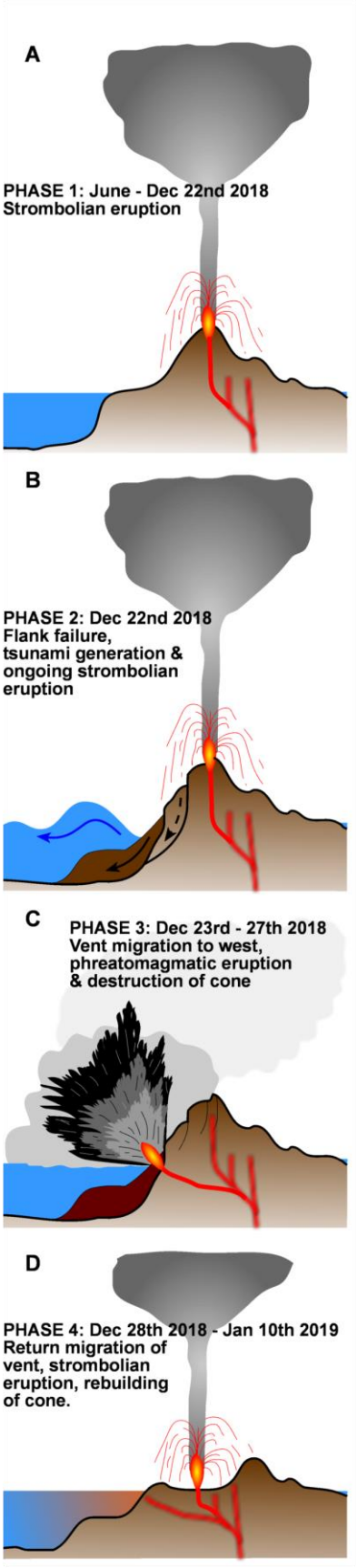

23 December 2018. It is this explosive activity that removed the remaining portion of the western flank and the summit of the volcano. Over the following three weeks, as new pyroclastic material and collapse material was added to the failed submarine structure, the vent migrated back toward its original location (Fig.1D-F, Fig. S3, Movies S1-S3). As new eruptive material was added, and the submarine flanks experienced smaller mass movements to recover a stable angle of repose, the stress regime on the plumbing system returned toward its earlier state, resulting in reactivation of the pre-failure magma pathway (Fig. 4).

Figure 4. Schematic time line of eruptive activity and tsunami generation at Anak Krakatau. Splayed magmatic plumbing in panel A represents an assumed migration of the vent prior to 2018 as interpreted from Fig. 3. The eruption plumes and tsunami are representative only and not to scale.

CONCLUSIONS

We describe a relatively small flank failure at Anak Krakatau that triggered a tsunami that had catastrophic consequences. The flank failure occurred during a normal, though heightened, eruptive episode, likely due to over steepening of the western flank on the edge of the 1883 caldera combined with alteration-related weakening of the deeper Anak-Krakatau stratigraphy. Thus, an extraordinary eruptive event was not required to trigger the tsunami. The satellite imagery taken ~8 hours after the tsunami clearly shows that the summit cone of the volcano is still intact, so volume calculations should not include this significant part of the edifice.

The volume of the flank failure was small, compared to predicted failure volumes and flank failures at other volcanoes, yet it generated a tsunami as large as and faster than modelled with a significantly larger failure. Significant regrowth of the island will be needed before flank failure is likely to occur again, but the underlying submarine architecture has been extensively remodelled. As a result, the failure criteria will be different for subsequent flank failures.

Establishing the new bathymetry and submarine stratigraphy following the 2018 flank failure is critical to strengthen the reliability of any future failure assessments of the volcano, and in understanding the hazard at other island volcanoes. Finally, this study also highlights that existing hazard assessments at volcanic islands are very likely underestimating the risks from volcanogenic tsunamis due to small (<0.25 km^3) failures.

ACKNOWLEDGMENTS

Earthquake locations and moment tensor solutions were obtained from the GEOFON programme of the GFZ German Research Centre for Geosciences using data from the GEVN partner networks. The authors thank Profs David Bond, Dan Parsons, Dave Petley, Drs Rachid

Omira, Budianto Ontowirjo, Jason Patton and Raphaël Paris for comments on an early draft and/or the pre-print of this manuscript. Two anonymous reviews improved the manuscript. Thank you to Dr Samuel Cheyney who compiled Fig. S2. Contributions: RW conceptualized the project, contributed to the formal analysis, investigation, methodology, validation and visualization and is responsible for the project administration and data curation. PR lead the formal analysis, investigation, methodology, validation and visualization. MG contributed to the formal analysis, investigation, validation and is responsible for the SAR processing. All authors discussed the results and contributed to the writing of the manuscript.

REFERENCES CITED

Agustan, Kimata, F., Pamitro, Y.E., and Abidin, H.Z., 2012, Understanding the 2007-2008 eruption of Anak Krakatau volcano by combining remote sensing technique and seismic data: International Journal of Applied Earth Observation and Geoinformation, v. 14, p. 73–82, doi:10.1016/j.jag.2011.08.011.

Andersen, Ø.L. Krakatau volcano: Witnessing the eruption, tsunami and the aftermath 22-23th December 2018: https://www.oysteinlundandersen.com/krakatau-volcano-witnessing-the-eruption-tsunami-22december2018/ (accessed January 2019).

Auker, M.R., Sparks, R.S.J., Siebert, L., Crosweller, H.S., and Ewert, J., 2013, A statistical analysis of the global historical volcanic fatalities record: Journal of Applied Volcanology, v. 2, p. 2–24, doi:10.1186/2191-5040-2-2.

BNPB Badan Nasional Penanggulangan Bencana Facebook:, https://www.facebook.com/HumasBNPB/ (accessed January 2019).

Bonaccorso, A., Calvari, S., Garfi, G., Lodato, L., and Patanè, D., 2003, Dynamics of the

December 2002 flank failure and tsunami at Stromboli volcano inferred by volcanological and geophysical observations: Geophysical Research Letters, v. 30, doi:10.1029/2003GL017702.

Camus, G., Gourgaud, A., and Vincent, P.M., 1987, Petrologic evolution of Krakatau (Indonesia): Implications for a future activity: Journal of Volcanology and Geothermal Research, v. 33, p. 299–316, doi:10.1016/0377-0273(87)90020-5.

Carracedo, J.C., 1999, Growth, structure, instability and collapse of Canarian volcanoes and comparisons with Hawaiian volcanoes: Journal of Volcanology and Geothermal Research, v. 94, p. 1–19, doi:10.1016/S0377-0273(99)00095-5.

Carracedo, J.C., Day, S.J., Guillou, H., and Pérez Torrado, F.J., 1999, Giant Quaternary landslides in the evolution of La Palma and El Hierro, Canary Islands: Journal of Volcanology and Geothermal Research, v. 94, p. 169–190, doi:10.1016/S0377-0273(99)00102-X.

Day, S.J., 2015, Chapter 58 - Volcanic Tsunamis, *in* Sigurdsson, H. ed., The Encyclopedia of Volcanoes (Second Edition), Amsterdam, Academic Press, p. 993–1009, doi:https://doi.org/10.1016/B978-0-12-385938-9.00058-4.

Decker, R., and Hadikusumo, D., 1961, Results of the 1960 expedition to Krakatau: Journal of Geophysical Research, v. 55, p. 3497–3511, doi:10.1029/JZ066i010p03497.

Deplus, C., Bonvalot, S., Dahrin, D., Diament, M., Harjono, H., and Dubois, J., 1995, Inner structure of the Krakatau volcanic complex (Indonesia) from gravity and bathymetry data: Journal of Volcanology and Geothermal Research, v. 64, p. 23–52, doi:10.1016/0377-0273(94)00038-I.

GEOFON Program, https://geofon.gfz-potsdam.de/eqinfo/event.php?id=gfz2018yzre (accessed February 2019).

Giachetti, T., Paris, R., Kelfoun, K., and Ontowirjo, B., 2012, Tsunami hazard related to a flank collapse of Anak Krakatau Volcano, Sunda Strait, Indonesia: Geological Society, London, Special Publications, v. 361, p. 79–90, doi:10.1144/SP361.7.

MAGMA Multiplatform Application for Geohazard Mitigation and Assessment in Indonesia:, https://magma.vsi.esdm.go.id/ (accessed February 2019).

Neumann van Padang, M., 1933, De Krakatau voorheen en Thans: De Tropische Natuur, v. 22, p. 137–150, http://natuurtijdschriften.nl/download?type=document&docid=511015 (accessed February 2019).

Pelinovsky, E.N., Zahibo, N., Dunkley, P., Edmonds, M., Herd, P., Talipove, T., Kozelkov, A., and Nikolkina, I., 2004, Tsunami generated by the volcano eruption on July 12-13, 2003 at Montserrat, Lesser Antilles: Science of Tsunami Hazards, v. 22, p. 44.

PVMBG Kementerian Energi dan Sumber Daya Mineral Badan Geologi:, http://www.vsi.esdm.go.id/ (accessed January 2019).

Ramadhan, P.B., 2018, Update Terkini Penanganan Bencana Tsunami Selat Sunda, Total 426 Orang Meninggal Dunia: TRIBUNnews, http://wartakota.tribunnews.com/2018/12/28/update-terkini-penanganan-bencana-tsunami-selat-sunda-total-426-orang-meninggal-dunia.

La Rocca, M., Galluzzo, D., Saccorotti, G., Tinti, S., Cimini, G.B., and Del Pezzo, E., 2004, Seismic signals asssociated with landslides and with a tsunami at Stromboli volcano, Italy: Bulletin of the Seismological Society of America, v. 94, p. 1850–1867,

doi:10.1785/012003238.

Self, S., and Rampino, M.R., 1981, The 1883 eruption of Krakatau: Nature, v. 294, p. 699–704, doi:10.1038/294699a0.

Di Traglia, F., Nolesini, T., Ciampalini, A., Solari, L., Frodella, W., Bellotti, F., Fumagalli, A., De Rosa, G., and Casagli, N., 2018, Tracking morphological changes and slope instability using spaceborne and ground-based SAR data: Geomorphology, v. 300, p. 95–112, doi:10.1016/j.geomorph.2017.10.023.

Voight, B., and Elsworth, D., 1997, Failure of volcano slopes: Géotechnique, v. 47, p. 1–31, doi:10.1680/geot.1997.47.1.1.

Watts, A.B., and Masson, D.G., 1995, A giant landslide on the north flank of Tenerife, Canary Islands: Journal of Geophysical Research: Solid Earth, v. 100, p. 24487–24498, doi:10.1029/95JB02630.

Supplementary information for

Reconstructing the Anak Krakatau flank collapse that caused the December 2018 Indonesian tsunami

Authors: Rebecca Williams[1]*, Pete Rowley[1], Matthew C. Garthwaite[2]
Affiliations: [1]Department of Geography, Geology & Environment, University of Hull, Hull, UK.
[2]Positioning and Community Safety Division, Geoscience Australia, Canberra, ACT, Australia.
*Correspondence to: Rebecca.williams@hull.ac.uk.

This supplementary information includes:

Figs. S1 to S3
Additional methods
Tables S1
Captions for Movies S1 to S3

Other Supplementary Information for this manuscript include the following:

Movies S1 to S3

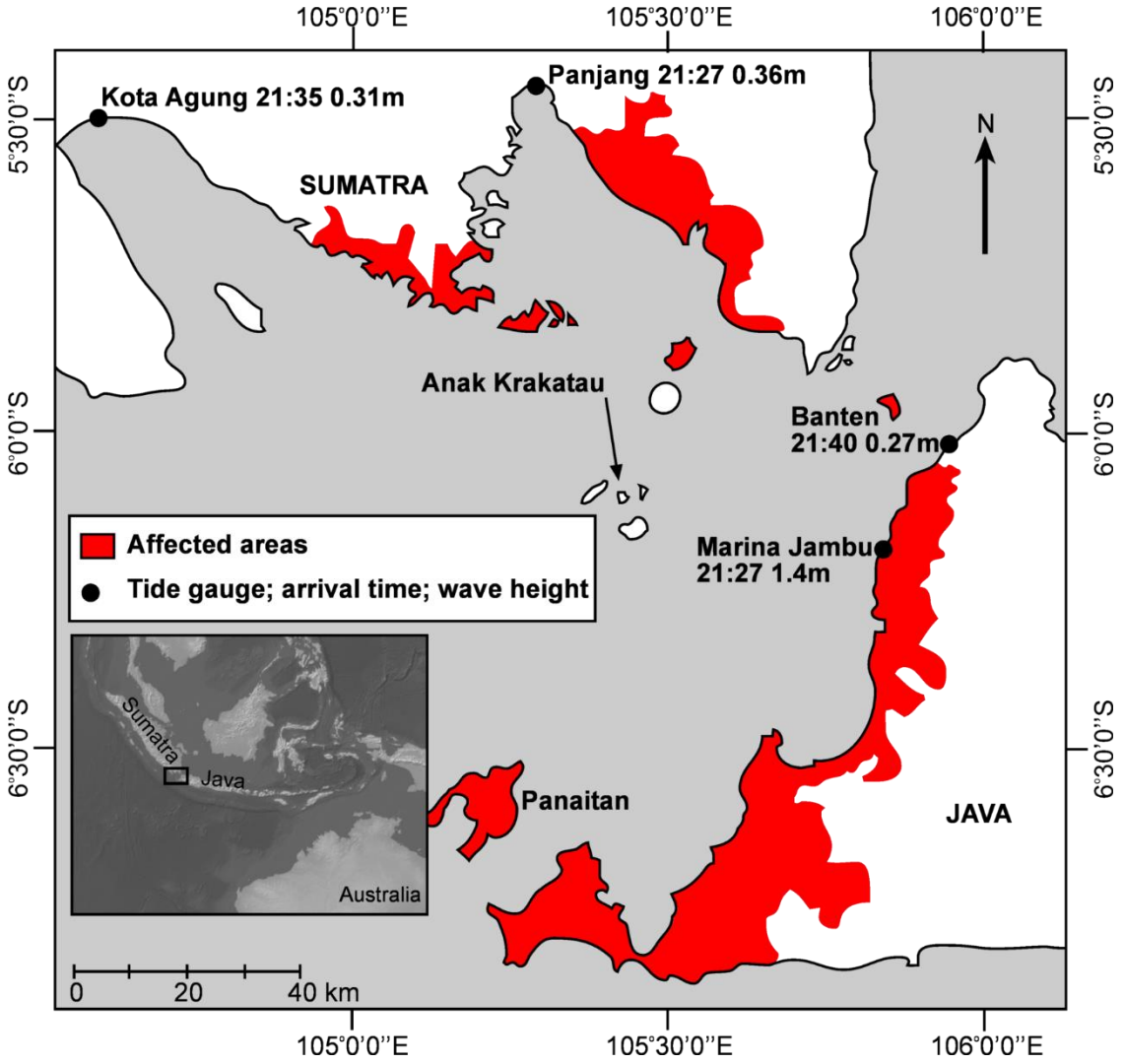

Fig. S1.

Location map of Anak Krakatau showing tide gauges in the Sunda Strait with wave arrival times and wave heights of the 22 December 2018 tsunami. Red zones show coastal subdistricts affected by the tsunami, adapted from Tsunami selat sunda provinsi Banten dan Lampung map created by Badan Nasional Penanggulangan Bencana dated 28 December 2018. Wave heights and arrival times given by Pusat Vulkanologi dan Mitigasi Bencana Geologi in a press release dated 24 December 2018.

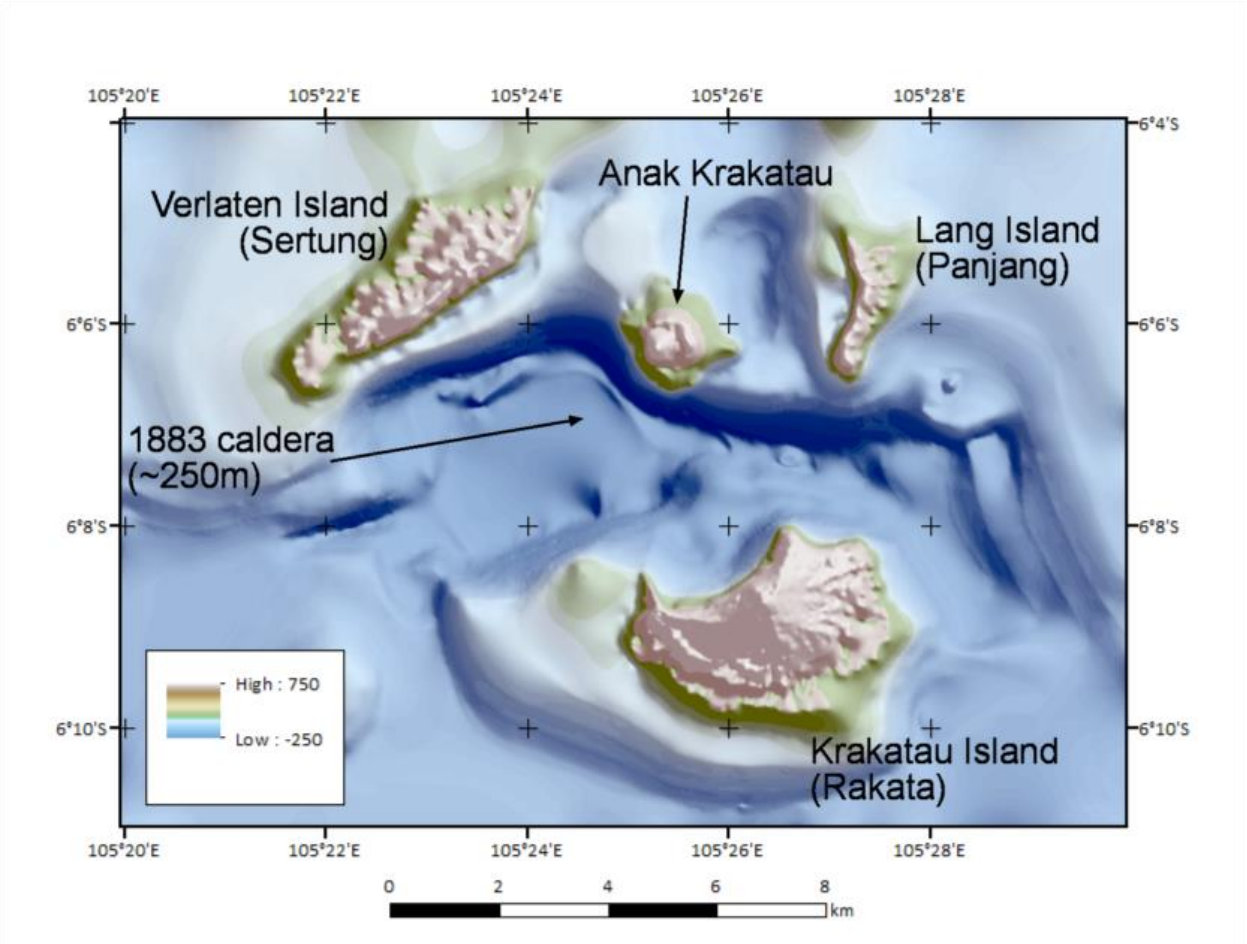

Fig. S2

Bathymentric map of the 1883 caldera, redrawn from Deplus et al., 1995.

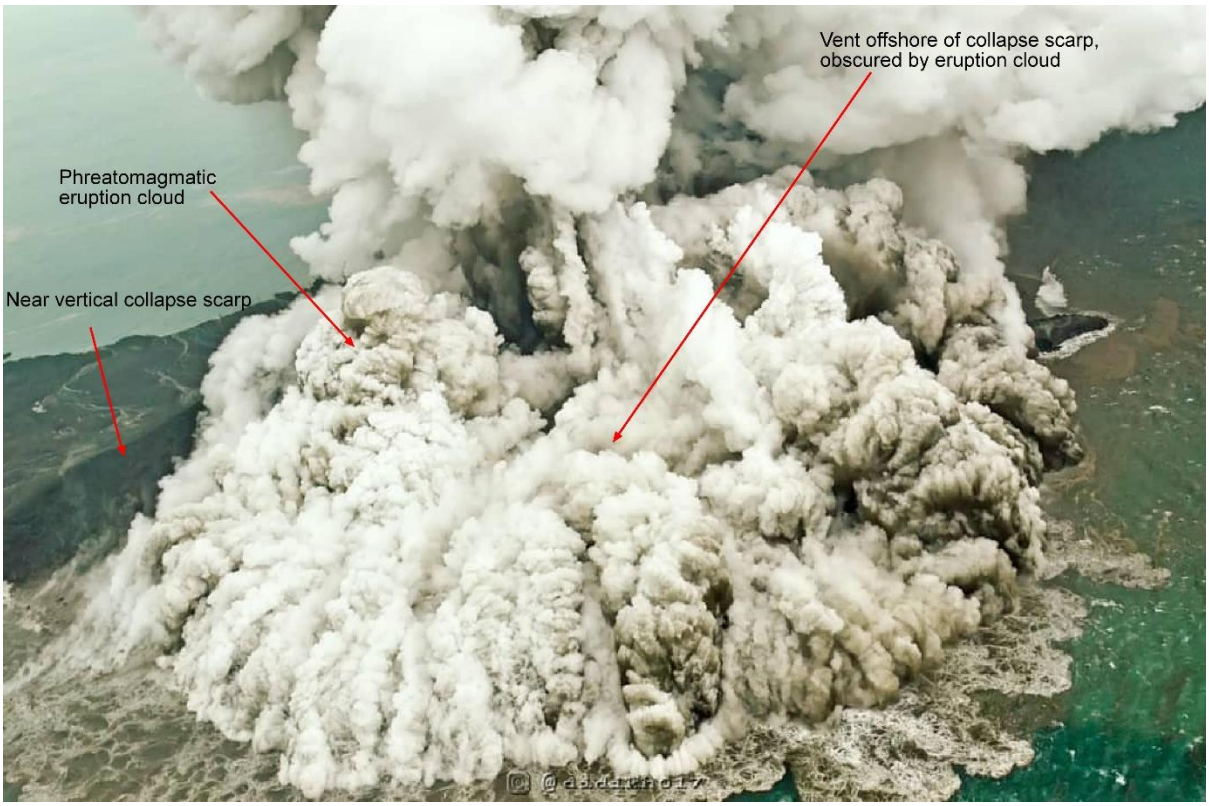

Fig. S3.

Image of the phreatomagmatic eruption taken on the 23 December 17:06 WIB. The steep scarp (near vertical) created by the flank failure can be seen behind the eruption plume (revealed to the left of the plume). Photo direction towards ESE. Image credit, used with permission: Instagram @didikh017

Methods

Synthetic Aperture Radar Processing

We obtained Sentinel-1 "Interferometric Wide Swath" (IWS) SAR products from the Copernicus Open Access Hub in three viewing geometries: two descending orbits and one ascending orbit (Table S1). Each SLC-format SAR product was converted to a "Sigma-0" backscatter coefficient image in slant-range geometry by applying the calibration and noise data annotated in the product metadata. We multi-looked (subsampled) the images to obtain approximately square pixels in radar geometry (4 range looks and 1 azimuth look).

A "master" image captured prior to the 22 December 2018 event was chosen for each of the three viewing geometries. Every other image within the three viewing geometry stacks (i.e. those not chosen as a "master") was then co-registered to its respective "master" image. Co-registration is the process of image alignment that involves measuring range and azimuth offsets between the two images via cross-correlation across a grid of sample windows covering the full image extents. A first-order polynomial transformation function is fitted (constant offset in range and azimuth directions) to the determined offsets and the image resampled to the radar-geometry of the "master" using a 2D Lanczos interpolation (of order 4). Every image was co-registered using an iterative procedure until the azimuth co-registration was better than 1/100 of a pixel. This high accuracy is particularly important if the Sentinel-1 IWS products are to be used for interferometry (not in this case). The result of this step is a stack of aligned radar-geometry images for each viewing geometry (Movie 1).

In a final step, the "master" image was used to derive a geocoding look-up table that can be used to transform the radar-geometry images to map view. This was done by first generating a

simulated radar backscatter image from the 1-arc-second (~30 m) SRTM Digital Elevation Model (DEM) covering the geographic extent of the radar image footprints. This simulated radar image was then transformed to radar geometry using the orbit information annotated in the "master" image's product metadata. Subsequent co-registration between this image and the "master" image was performed to enable a refinement of the transformation parameters to be undertaken. Sentinel-1 image products usually only need a first-order polynomial transformation owing to the high quality of the provided orbit information. The Sentinel-1 image products we have used cover a much larger area than just the Krakatau caldera and include large portions of Java and/or Sumatra. Therefore the accuracy of the co-registration of the "master" images to the simulated radar image is not affected by the highly localised changes occurring at Anak Krakatau between image captures. A refined geocoding look-up table was then derived that provides a transformation to map view for every pixel in the radar-geometry image.

Finally, all radar-geometry images in each viewing geometry were orthorectified using the look-up table. A B-spline interpolation (of order 5) was used to perform the resampling.

Sentinel 2 Data

We obtained Sentinel 2A true colour images (TCI) collected on the 16th November 2018 from the Copernicus Open Access Hub.

DEM

We obtained a 0.27-arc-second resolution DEM from the Indonesian Geospatial Agency (Badan Informasi Geospasial). This DEM, covering the whole of Indonesia, was constructed from data from TerraSAR-X (from 2011 - 2013), InSAR (from 2000, 2004, 2008, and 2011) and ALOS-PALSAR (2007/2008) (pers. comm. Susilo Sarimun, Badan Informasi Geospasial, 7th February

2019). The heights given in the DEM are therefore relevant to an epoch sometime between 2000 and 2013. The DEM was converted to a triangulated irregular network (TIN), after resampling to a higher resolution grid.

Data availability

The Sentinel datasets analysed during the current study are available in the Copernicus Open Access Hub, https://scihub.copernicus.eu/. The DEM analysed is available from the Indonesian Geospatial Agency (Badan Informasi Geospasial) (http://tides.big.go.id/DEMNAS/#Info). Processed datasets generated during the current study are available from the corresponding author on reasonable request.

Table S1.

Details of the Sentinel-1 SAR images used in this study. Elevation and Azimuth angles are for a looking vector towards the satellite originating at the summit cone of Anak Krakatau prior to the flank failure and tsunami. Italicised entries denote images captured before the 22 December 2018 event occurred.

Relative orbit	Pass	Satellite	Acquisition Date (UTC)	Time (UTC)	Days since previous	Elevation (deg)	Azimuth (deg)
171	*Ascending*	*S1A*	*7/12/2018*	*11:23:07*	-	*46.9*	*257.5*
171	*Ascending*	*S1A*	*19/12/2018*	*11:23:06*	*12*	*46.9*	*257.5*
171	Ascending	S1B	25/12/2018	11:22:35	6	46.9	257.5
171	Ascending	S1A	31/12/2018	11:23:06	6	46.9	257.5
171	Ascending	S1A	12/1/2019	11:23:05	12	46.9	257.5
47	*Descending*	*S1A*	*28/11/2018*	*22:33:45*	-	*45.1*	*102.6*
47	*Descending*	*S1A*	*10/12/2018*	*22:33:45*	*12*	*45.1*	*102.6*
47	Descending	S1A	22/12/2018	22:33:44	12	45.1	102.6
47	Descending	S1B	28/12/2018	22:33:06	6	45.1	102.6
47	Descending	S1A	3/1/2019	22:33:44	6	45.1	102.6
47	Descending	S1A	15/1/2019	22:33:44	12	45.1	102.6
120	*Descending*	*S1A*	*3/12/2018*	*22:41:39*	-	*58.6*	*102.3*
120	*Descending*	*S1A*	*15/12/2018*	*22:41:39*	*12*	*58.6*	*102.3*
120	Descending	S1A	27/12/2018	22:41:38	12	58.6	102.3
120	Descending	S1B	2/1/2019	22:41:04	6	58.6	102.3
120	Descending	S1A	8/1/2019	22:41:38	6	58.6	102.3
120	Descending	S1A	20/1/2019	22:41:38	12	58.6	102.3

Movie S1.

Animated compilation of Sentinel-1 SAR backscatter images in the native radar viewing geometry (T120D). Annotated labels give the viewing geometry (relative orbit and pass direction) and the image capture date (UTC). Image x-axis is the range direction and y-axis is the azimuth, or along-track direction of the radar viewing geometry. Details of the three viewing geometries are given in Table S1.

Movie S2.

Animated compilation of Sentinel-1 SAR backscatter images in the native radar viewing geometry (T171A). Annotated labels give the viewing geometry (relative orbit and pass direction) and the image capture date (UTC). Image x-axis is the range direction and y-axis is the azimuth, or along-track direction of the radar viewing geometry. Details of the three viewing geometries are given in Table S1.

Movie S3.

Animated compilation of Sentinel-1 SAR backscatter images in the native radar viewing geometry (T047D). Annotated labels give the viewing geometry (relative orbit and pass direction) and the image capture date (UTC). Image x-axis is the range direction and y-axis is the azimuth, or along-track direction of the radar viewing geometry. Details of the three viewing geometries are given in Table S1.